Investigation of magnetic inhibition effect on ion acceleration at high laser intensities

View Online Export Citation CrossMark

H. Huang, Z. M. Zhang,[a] (iD) B. Zhang, W. Hong, S. K. He, (iD) L. B. Meng, W. Qi, B. Cui, and W. M. Zhou[a] (iD)

AFFILIATIONS

Science and Technology on Plasma Physics Laboratory, Mianyang 621900, China

[a]Authors to whom correspondence should be addressed: zmzhang_zju@sina.com and zhouwm@caep.cn

ABSTRACT

The irradiation of a target with high laser intensity can lead to self-generation of an intense magnetic field (B-field) on the target surface. It has therefore been suggested that the sheath-driven acceleration of high-energy protons would be significantly hampered by the magnetization effect of this self-generated B-field at high enough laser intensities. In this paper, particle-in-cell simulations are used to study this magnetization effect on sheath-driven proton acceleration. It is shown that the inhibitory effect of the B-field on ion acceleration is not as significant as previously thought. Moreover, it is shown that the magnetization effect plays a relatively limited role in high-energy proton acceleration, even at high laser intensities when the mutual coupling and competition between self-generated electric (E-) and B-fields are considered in a realistic sheath acceleration scenario. A theoretical model including the $v \times B$ force is presented and confirms that the rate of reduction in proton energy depends on the strength ratio between B- and E-fields rather than on the strength of the B-field alone, and that only a small percentage of the proton energy is affected by the self-generated B-field. Finally, it is shown that the degraded scaling of proton energy at high laser intensities can be explained by the decrease in acceleration time caused by the increased sheath fields at high laser intensities rather than by the magnetic inhibitory effect, because of the longer growth time scale of the latter. This understanding of the magnetization effect may pave the way to the generation of high-energy protons by sheath-driven acceleration at high laser intensities.

I. INTRODUCTION

Laser-driven ion acceleration has been the focus of much research activity for several decades because of its potential to provide compact energetic ion sources with unique beam properties, including short duration, high brilliance, and low emittance. These favorable characteristics of laser-produced ion beams make them very appealing for many applications, such as ion-beam tumor therapy,[1,2] proton radiography,[3] production of warm dense matter,[4] and fast ignition of fusion targets.[5–7] However, an important requirement for several of these applications is an increase in the energy per nucleon up to hundreds of MeV and beyond, which is also the major challenge facing current laser-driven ion sources.[8–10]

The most widely investigated ion acceleration mechanism in the laboratory is target normal sheath acceleration (TNSA).[11,12] In this scheme, the ions are accelerated to high energies by electrostatic fields at the rear side of a thin target foil, which are produced by the super-thermal electrons generated at the laser-irradiated side. Recently, TNSA proton energies in excess of 85 MeV from ultrathin foils have been reported,[13] and attempts have been made to achieve higher proton

energies in excess of 100 MeV by raising the laser intensity.[14] However, a recent study by Nakatsutsumi *et al.*[15] indicated that the laser-driven sheath acceleration of high-energy protons would be inhibited by self-generated surface magnetic fields (B-fields).

An intense B-field is inevitably self-generated on the surface of a target irradiated by a high laser intensity. Recent experimental studies of self-generated B-fields in high-intensity laser–solid interactions using either ultrafast electron or proton radiography have shown that B-fields with strengths of tens of megagauss (MG) can grow in a few hundreds of femtoseconds for $I_L\lambda_L^2 \leq 10^{19}$ W μm^2 cm^{-2}, and B-fields of the order of 100 MG have been observed during the irradiation of targets with laser intensities beyond 10^{20} W μm^2 cm^{-2}.[16–18] In such extreme B-fields, the sheath electrons are thought to be highly magnetized, i.e., they are scattered away from the sheath axis owing to $E \times B$ drift and become trapped on the target surface. As a result, the electron sheath is shortened and the electric field (E-field) strength is decreased owing to the reduced longitudinal electron pressure and density, thus reducing the maximum energy that the ions can acquire, as discussed by Nakatsutsumi *et al.*[15] However, the analysis presented

by the latter authors relies for the most part on the physical picture discussed above and is thus rather qualitative. As a result, especially for realistic TNSA scenarios, there is a lack of any quantitative estimates of magnetization effects on sheath-driven ion acceleration, for example, estimates of how much the ion energy can be reduced by a self-generated B-field. Therefore, more effort is needed to understand the effect of self-generated B-fields on ion acceleration at high laser intensities.

In this paper, using a two-dimensional (2D) particle-in-cell (PIC) code, we investigate the magnetization effect on ion acceleration. An external magnetic field with strength proportional to that of the self-generated B-field is added to the simulation. This allows the effect of the self-generated B-field to be modified, thus providing a direct comparison of the magnetization effects of self-generated B-fields of different strengths.

As well as the PIC simulations, a simplified TNSA model including the $v \times B$ force is also presented in order to provide a relatively quantitative estimation of the magnetization effect on sheath-driven ion acceleration. Finally, further PIC simulations are performed to examine the scaling of proton energy at high laser intensities, for which the magnetization effect has previously been thought to be dominant. It is shown here that the magnetization due to the self-generated B-field in a realistic TNSA scenario has only a limited effect on high-energy proton acceleration. The degraded scaling of proton energy at high laser intensities is also shown to be the result of a decrease in acceleration time due to the increased sheath field, rather than to the inhibitory effect of the intense self-generated B-field.

II. PARTICLE-IN-CELL SIMULATIONS

To simulate the ion acceleration from intense laser irradiation of a solid target, we turn to PIC simulation codes, which allow a first-principles description of laser–plasma interaction. If the target is sufficiently thick that the laser cannot penetrate through it, particles at the rear side experience only self-generated electromagnetic fields, i.e., the particle momentum equation is

$$\frac{dP}{dt} = q\left(E_s + \frac{1}{c} v \times B_s\right), \tag{1}$$

where E_s and B_s are the self-generated sheath E- and B-fields respectively, c is the speed of light and q is the charge of the particle. The magnetization effect described here arises mainly from the fact that both the electrons and ions at the rear side are deflected and/or trapped by the self-generated B-field. Therefore, the significance of the magnetization effect in inhibiting ion acceleration depends mostly on the Lorentz force, i.e., $v \times B_s$, on the high-energy electrons and ions (which escape to the vacuum) caused by the self-generated B-field B_s at the rear side of the target. An external B-field B_{ex} is therefore adopted to provide an artificial modification of the magnetization effect. Since it is the magnetization effect of the self-generated B-field that is of most interest here, the external B-field is carefully set to be consistent with the self-generated B-field in both strength and spatial distribution at every time step in our simulations. This modification has little effect on either the laser absorption or the hot-electron generation at the front side of the target, but it does have an impact on the dynamics of the particles at the rear side, thus providing a means of evaluating the magnetization effects of self-generated B-fields with different strengths.

The two-dimensional (2D) PIC simulations in this work are performed using the code named OPIC.[19] The simulation box is 160λ (x) $\times$ 120λ (y) (λ is the wavelength of the incident laser), decomposed into a grid with 8000×4000 cells. The P-polarized laser beam incident from the left boundary has a spatial–temporal profile given by $a = a_0 \exp(r^2/w^2) \sin(\pi t/2\tau)$ ($0 < t < 2\tau$, $r^2 = x^2 + y^2$), where $a_0 = eE_0/m_e\omega c = 100$ (ω is the angular frequency of laser and corresponds to a peak intensity $I = 1.37 \times 10^{22}$ W cm^{-2} for the assumed wavelength $\lambda = 1$ μm), $w = 5\lambda$, and $\tau = 50T_0$ ($T_0 = \lambda/c$ is the laser period). The target is fully ionized, consisting of a neutral plasma of electrons and Al^{13+} ions. A 20 nm thick layer of protons is attached to the rear side of the target to mimic surface contaminants. The electron densities of both the Al target and proton layer are set to $260n_c$, where $n_c = 1.12 \times 10^{21}$ cm^{-3} is the critical density. The initial temperatures of the electrons and ions are set to 1 keV. The target is initially located at $x = 10$ μm, with a thickness of 15 μm. The target plasma and the layer contain 64 and 100 simulation particles per cell for each species, respectively. To suppress numerical heating, high-order (fourth) interpolation is adopted for the simulation particles. An absorbing boundary condition is used for both the electromagnetic fields and the simulation particles.

The use of a relatively thick target (15 μm) in our simulations is to ensure that a pure TNSA scenario occurs at the rear side of the target. In this thick-target case, the hole-boring of the ultra-intense laser cannot reach the target rear side, i.e., the intense laser pulse cannot penetrate through the target during the whole interaction. The energetic particles at the rear side of the target escape into the vacuum and thus only experience the self-generated E- and B-fields, making it possible to clearly identify the magnetic inhibition effect. A moderate pulse duration of 165 fs is also adopted here to prevent self-induced transparency of the target even at the maximum laser intensity of 7×10^{22} W cm^{-2} used for the scaling study (see Sec. IV). In fact, we have also performed simulations with longer pulse durations of, for example, 330 fs. The simulation results on the inhibitory effect of magnetization are consistent with those in the case of relatively short pulse duration. The spatial resolution in the simulation is $dx = 0.02$ μm, $dy = 0.03$ μm, and these values are much smaller than the initial skin depth given by $l_s = c/\omega'_P \approx 0.7$ μm, where $\omega'_P = (4\pi e^2 n_0/\langle\gamma\rangle m_e)^{1/2}$ is the relativistic corrected plasma frequency and $\langle\gamma\rangle = (1 + a_0^2/2)^{1/2}$ is the relativistic factor for a linearly polarized laser. The initial Debye length is given by $\lambda_D = (T_e/4\pi n_0 e^2)^{1/2} \approx 4.3 \times 10^{-4}$ μm. Although the spatial resolution in our simulation is much larger than the initial Debye length, little numerical heating is observed, for the following two reasons. First, the electrons are soon heated up to MeV temperatures during irradiation of the target by the ultra-intense laser, resulting in a much larger Debye length that becomes comparable to the grid size. Second, the use of high-order (fourth) interpolation for the simulation particles is very effective in extending the grid size beyond the Debye length without numerical heating. We have also performed simulations with a higher spatial resolution of $dx = dy = 0.01$ μm, and the simulation results are convergent, indicating that the spatial resolution is high enough for the present study.

To compare the magnetization effect at different B-field strengths, we perform simulations with three different external B-fields $B_{ex} = mB_s$, with $m = -1$, 0, and 4, referred to as cases I, II, and III, respectively. These external B-fields are applied such that the energetic particles escape into the vacuum region at the rear side of the target, which can be simply achieved by an appropriate initial position

of the rear surface of the target, namely, in the region $x \geq 25.02 \, \mu$m. In case I, the charged particles at the rear side experience a modified B-field $\boldsymbol{B}_m = \boldsymbol{B}_{ex} + \boldsymbol{B}_s = 0$ such that the Lorentz force on the charged particles is exactly zero, i.e., the magnetization effect vanishes completely. Case II is the normal TNSA case with $\boldsymbol{B}_m = \boldsymbol{B}_s$. In case III, $\boldsymbol{B}_m = 5 \, \boldsymbol{B}_s$, leading to an enhancement of the magnetization effect by a factor of 5.

The energy spectra of the accelerated protons for the three cases at $t = 100 T_0$ are shown in Fig. 1(a). We can see that there is very little difference in the maximum energies of the protons between cases I and II, suggesting that the magnetization effect indeed plays a rather limited role in the high-energy proton acceleration, especially for the highest-energy protons. This can be explained physically as follows. On the one hand, it should be noted that because of the competition between the electric and magnetic effects on the proton acceleration, the reduction in proton energy depends on the strength ratio between $\boldsymbol{B}_s$ and $\boldsymbol{E}_s$ rather than on the strength of $\boldsymbol{B}_s$ alone. According to the analytical model described in Sec. III, the rate of reduction in the proton energy is expected to be small, i.e., $\delta \mathcal{E}_i / \mathcal{E}_i \leq 10\%$ (where $\mathcal{E}_i$ is the ion energy), in a realistic TNSA scenario. On the other hand, in general, the B-field has a longer growth time than the sheath E-field.[20,21] Thus, the highest-energy protons are accelerated promptly before the B-field grows to a sufficiently high level that the magnetization effect becomes important. In addition, since the highest-energy protons propagate nearly along the laser axis, where the B-field is weak, they are deflected only slightly by the B-field. As a result, there is very little difference in the maximum energies of protons between the nonmagnetization and magnetization cases. By comparison, a reduction in the maximum energy of accelerated protons from 240 to 180 MeV is observed in case III, for which the magnetization effect is artificially enhanced. The time evolution of the laser-to-proton energy conversion efficiency (CE) for the three cases is also presented in Fig. 1(b). The impact of the magnetization effect on CE is similar to that on the maximum proton energy. That is, a significant reduction of 20% in CE is observed in case III, while there is little difference between cases I and II. These results confirm that the magnetization effect can indeed play a role in inhibiting ion acceleration, but the self-generated B-fields in realistic TNSA scenarios do not appear to be strong enough to significantly reduce either the maximum energy or the conversion efficiency of the accelerated protons.

The magnetization effect on proton dynamics can be seen more clearly by inspecting the proton angular distributions in Figs. 2(a)–2(c). For all three cases, a hollow ring structure at low proton energies is observed. It is interesting to see from a comparison of the ring diameters that the divergence of the low-energy protons is greatest in case I, for which the magnetization effect is completely inhibited. This is in contrast to the expectation that the self-generated B-field will lead to a greater deflection of the accelerated protons. In fact, the increased divergence of the protons in the nonmagnetization case can be explained as follows. As the ions are accelerated by the sheath field, the rear surface of the target is deformed, becoming curved as depicted in Figs. 2(d)–2(f), owing to the plasma expansion. This curvature of the rear surface results in the generation of a transverse component of the sheath field, $E_y = \partial(n_e k T_e)/\partial y$. In the absence of the magnetization effect, E_y can grow to a high level, as shown in Fig. 2(g), thus strongly deflecting the accelerated ions. Instead, in the presence of the magnetization effect, the hot electrons become highly magnetized, i.e., they perform gyro-motion on the target surface with a Larmor radius $r_B = \gamma m_e v_e / eB$. This gyro-motion of the hot electrons tends to inhibit the generation of the transverse sheath field E_y, as shown in Figs. 2(h) and 2(i). As a result, the protons in the magnetized case are less deflected by the transverse sheath field, and thus exhibit a much smaller divergence. When the magnetization effect is enhanced, i.e., in case III, the proton divergence is found to increase slightly, owing to the enhanced deflection by the increased $\boldsymbol{v} \times \boldsymbol{B}$ force. Finally, the highest-energy protons in all three cases exhibit the standard bell-shaped profile expected for TNSA. This is because these protons are accelerated on axis, where both B_z and E_y vanish, and thus they are less deflected by these fields.

The spatial distributions of the self-generated B-fields at $t = 75 T_0$ in the three cases are shown in Figs. 2(j)–2(l). It should be noted that the escaping electrons and ions actually experience the modified B-field $\boldsymbol{B}_m = \boldsymbol{B}_{ex} + \boldsymbol{B}_s$, which is different from the self-generated B-field. It is found that in case I, the self-generated B-field at the rear side grows to the highest strength. This is because in this case without magnetic deflection, the expansion of the rear side of the target is much more homogeneous, which results in a sharper boundary between the rear side and the vacuum. That is, the gradients of both the electron density and electron temperature there are increased. As a result, the generation of the B-field by the Biermann battery mechanism,[22] i.e., $(\nabla T_e \times \nabla n_e)/n_e e$, is reinforced. By contrast, in the other
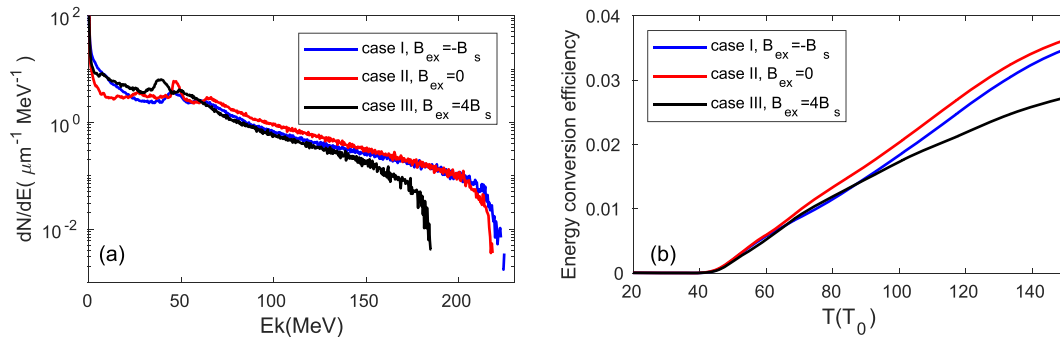

FIG. 1. (a) Proton energy spectra for cases I (blue), II (red), and III (black) at $t = 100 T_0$ (T_0 is the laser period). (b) Laser-to-proton energy conversion efficiency as a function of simulation time.

two cases, the hot electrons are highly magnetized, i.e., they perform gyro-motion with a small radius at the rear side of the target. Since these hot electrons are tightly bound at the rear side, the heat exchange between the hot and cold electrons there is reinforced, leading to local thermal diffusion. As a result, both the electron temperature and density gradients are decreased. The generation of the B-field in these two magnetized cases is thus relatively inhibited. Also, filamentary

structures can clearly be observed in the self-generated E- and B-fields in the magnetized cases [see Figs. 2(g)–2(l)]. In fact, these filamentary structures result mainly from the Weibel instability caused by interpenetration of the forward and return electron currents.[23] The weaker development of filamentary field structures in case I can be attributed to the fact that in this case both the forward and return electron currents (i.e., the motions of electrons) at the rear side are
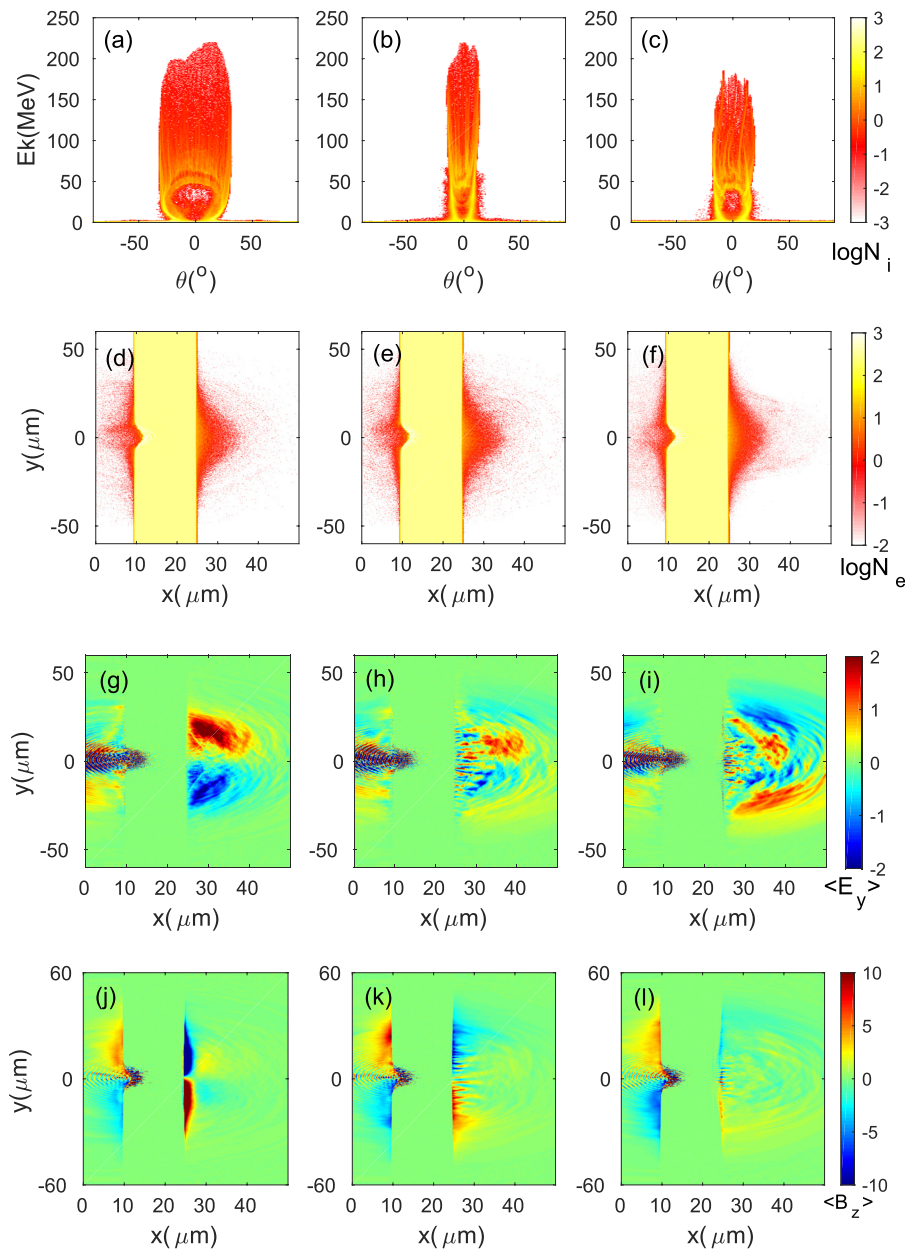

FIG. 2. (a)–(c) Proton angular distributions at $t = 100T_0$ for cases I–III, respectively. (d)–(f) Spatial distributions of electron density n_e at $t = 75T_0$ for cases I–III, respectively. The corresponding spatial distributions of the averaged transverse electric field $\langle E_y \rangle$ and self-generated azimuthal B-field $\langle B_z \rangle$ are shown in (g)–(i) and (j)–(l), respectively. Here $\langle \; \rangle$ denotes the average over one laser period T_0, e.g., $\langle E_y \rangle = (1/T_0) \int_{t-T_0/2}^{t+T_0/2} E_y(t)\,dt$. The line $y = 0$ corresponds to the laser axis.

decoupled from the self-generated B-field. The presence of filamentary structures in the magnetized cases indicates that the growth in the magnetic field by the Biermann battery mechanism is inevitably destroyed by the Weibel instability. This results in a decrease in the strength of the self-generated B-field, thus reducing the magnetized inhibition of proton acceleration.

It is known that sheath field evolution is dominated by the collective dynamics of hot electrons at the rear side.[11] To investigate hot-electron dynamics under different magnetization conditions, the time-integrated spectra of the forward and backward electrons as they pass by the boundaries placed at the rear side of the target ($x = 26\,\mu m$) are calculated, with the results shown in Fig. 3. It can be observed that the spectra of the forward electrons are nearly identical for the three cases, indicating that the generation of hot electrons at the front side of the target is little affected by modification of the magnetization conditions at the rear side. It can thus be expected that these hot electrons escape into the vacuum to generate the same sheath fields at the rear side of the target for all three cases. Owing to reflection by both the sheath E- and B-fields, these hot electrons return to the target, and the sheath fields thus become weaker. As can be seen in Fig. 3(b), the return (backward) electrons in cases I and II have nearly the same spectra, which may be because the backward hot electrons are dominated by the sheath E-field rather than by the self-generated B-field since the magnetization effect is small in realistic TNSA scenarios. In case III, however, it can be seen that many more electrons with high energies are reflected, owing to the enhanced magnetization effect. The enhancement of the returning electrons in this case finally results in more weakening of the sheath field, thus giving rise to a significant reduction in the maximum energy of accelerated protons, as observed in Fig. 1.

To clearly reveal the dynamics of the accelerated protons under different magnetization conditions, we examine the trajectories of two sample protons. The first sample proton is initially located at the position ($25.02, 0\,\mu m$) corresponding to the highest-energy protons accelerated on the axis, where $y = 0$ corresponds to the laser axis. As shown in Fig. 4(a), the on-axis protons for all three cases are accelerated along the central axis. There is little deflection, since the B_z and E_y fields vanish on the axis. As can be seen in Fig. 4(b), the longitudinal sheath field E_x experienced by the on-axis proton in case I
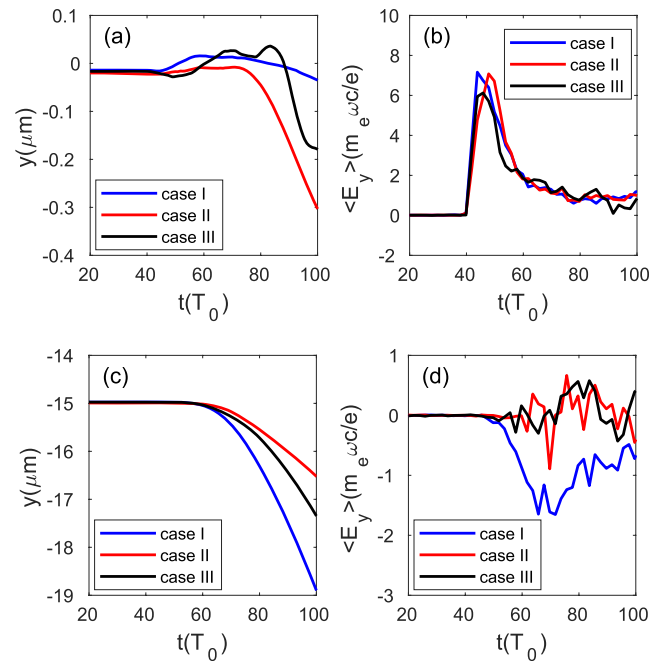
FIG. 4. (a) and (b) Evolution of an on-axis proton initially located at ($25.02, 60\,\mu m$): (a) transverse position y; (b) averaged longitudinal sheath field $\langle E_x \rangle$. (c) and (d) Evolution of an off-axis proton initially located at ($25.02, 45\,\mu m$): (c) transverse position y; (d) averaged transverse sheath field $\langle E_y \rangle$. $\langle\,\rangle$ denotes the average over one laser period. The line $y = 0$ corresponds to the laser axis.

is almost same as that in case II, indicating that the accelerating field is not affected much by the presence of the surface B-field generated in a realistic TNSA scenario. However, in case III, the on-axis sheath field is reduced both in strength and spatial scale, resulting in a lower proton energy gain. The inhibition of the sheath field in this case can be attributed to the strongly magnetized electrons drifting away from the center of the sheath, as will be discussed in Sec. III.
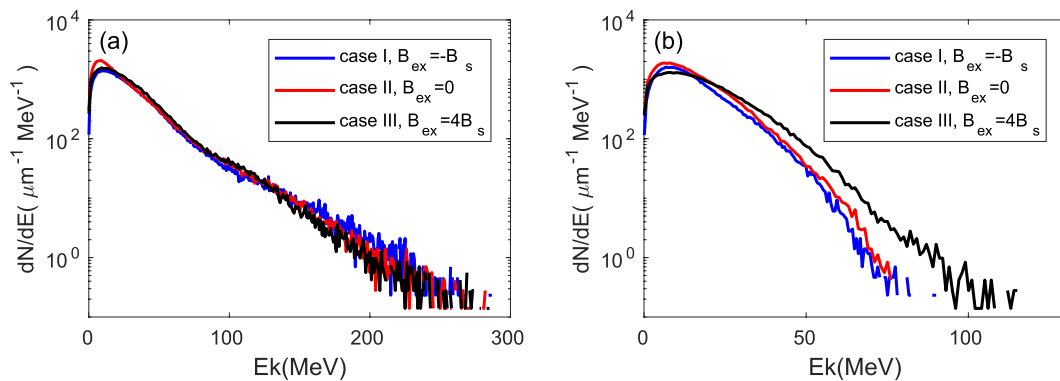
FIG. 3. Time-integrated spectra of (a) the forward and (b) the backward electrons as they pass by the boundaries placed at the target rear side ($x = 26\,\mu m$) at $t = 75T_0$.

We also track another proton initially located at the off-axis position (25.02, −15 μm) where the self-generated B-field is most intense. Figure 4(c) shows that the off-axis proton is deflected outward in all three cases, i.e., toward regions where the sheath field is lower. In fact, it is found that the off-axis proton in case I is deflected mostly by the transverse electric field E_y, while in the other two cases it is deflected mostly by the azimuthal B-field B_z because in these two cases E_y is strongly inhibited [see Fig. 4(d)]. Since low-energy protons are strongly deflected by E_y in the non-magnetized case, they have a larger divergence than in the magnetized case, as is observed in Fig. 2.

III. ANALYTICAL MODEL OF MAGNETIZATION EFFECT

Many theoretical models have been proposed to describe ion acceleration in the TNSA scenario.[24–27] In most of these models, the system is described as a neutral plasma consisting of hot electrons, in which the ions acquire kinetic energies in the course of sheath evolution. This approach is therefore similar to the classic description of plasma expansion into vacuum.[20,28,29] An analytical solution for the plasma expansion can be found in the quasineutral approximation using a self-similar theory. Two interpolation formulas for the electric field and ion velocity at the ion front were obtained by Mora using a Lagrangian fluid code.[20] In all of these models, however, a 1D geometry, consistent with the electrostatic assumption, is usually adopted, while the influence of the self-generated B-field is neglected. Here, an extended TNSA model including the $\boldsymbol{v} \times \boldsymbol{B}$ force is presented to estimate the rate of reduction in ion energy caused by the self-generated B-field.

In the presence of the self-generated B-field, the electrons at the rear of the target become magnetized and drift away from the center of the sheath under the action of the $\boldsymbol{v} \times \boldsymbol{B}$ force, thus resulting in inhibition of both the sheath field and the proton acceleration. To model this effect, we first consider the motion of the magnetized electrons in cylindrical coordinates, with the laser pulse incident along the z direction. For simplicity, we assume that the variation of all physical quantities in the transverse direction is much smaller than that in the longitudinal direction, i.e., $\partial/\partial r \ll \partial/\partial z$. This quasi-1D assumption is justified provided that the lateral extent of the sheath is much greater than the acceleration length of the protons. Therefore, the longitudinal sheath electric field and the azimuthal magnetic field can be expressed as $\boldsymbol{E} = \boldsymbol{E}_z(z,t)\hat{\boldsymbol{z}}$ and $\boldsymbol{B} = \boldsymbol{B}_\theta(z,t)\hat{\theta}$, respectively. Using the relations $E_z = -\partial\phi/\partial z$ and $B_\theta = (\nabla \times A)_\theta \simeq \partial A_r/\partial z$, the distribution function $f^e(z, v_z, t)$ of the electrons is governed by the Vlasov equation

$$\frac{\partial f^e}{\partial t} + v_z \frac{\partial f^e}{\partial z} + \frac{e}{m_e}\left(\frac{\partial \phi}{\partial z} - v_r \frac{\partial A_r}{\partial z}\right)\frac{\partial f^e}{\partial v_z} = 0. \quad (2)$$

Following Mora and Pellat,[28] we rewrite all the dependent and independent variables in dimensionless form: $z = z/c_s t_0$, $t = t/t_0$, $v = v/v_t$, $\phi = e\phi/T_e$, and $A = eA/T_e v_t$, where $c_s = (ZT_e/m_i)^{1/2}$ is the ion sound speed and $v_t = (T_e/m_e)^{1/2}$ is the electron thermal velocity. Substituting these expressions into Eq. (2), we write

$$\frac{\partial f^e}{\partial t} + R v_z \frac{\partial f^e}{\partial z} + R\left(\frac{\partial \phi}{\partial z} - v_r \frac{\partial A_r}{\partial z}\right)\frac{\partial f^e}{\partial v_z} = 0, \quad (3)$$

where $R = v_t/c_s = (m_i/Z m_e)^{1/2}$. If we assume the electrons to be in equilibrium with the slowly varying electric and magnetic fields, we

can neglect $\partial f^e/\partial t$ in Eq. (3). Using the self-similar variable $\xi = z/t$, this equation is further simplified as

$$v_z \frac{\partial f^e}{\partial \xi} + \frac{\mathrm{d}(\phi - v_r A_r)}{\mathrm{d}\xi}\frac{\partial f^e}{\partial v_z} = 0. \quad (4)$$

This is similar to Mora's original result, apart from a magnetization term arising from the self-generated B-field.

Integration of Eq. (4) gives

$$f^e(v_z, \xi) = f_0\left(\left[v_z^2 - 2(\phi - v_r A_r)\right]^{1/2}\right), \quad (5)$$

where $f_0(u)$ is the electron distribution function in the unperturbed plasma ($\phi = A_r = 0$). Generally, the hot electrons generated from the interaction of an intense laser beam with a solid target move primarily along the longitudinal direction and have a Maxwellian distribution with a characteristic temperature. In the presence of a B-field, these electrons will be deflected, giving rise to a considerable perpendicular velocity v_r. To simplify the analysis, we neglect the variation of the perpendicularly velocity. We assume a Maxwellian function and a delta function for the longitudinal and perpendicular velocity distributions of the hot electrons, respectively,[30] i.e., $f_0(v_z, v_r) = \exp(-v_z^2/2)\delta(v_r = v_{r0})$, where v_{r0} is the average value of the perpendicular velocity. Therefore, the electron density is obtained as

$$n_e = n_{e0}\exp(\phi - v_{r0}A_r). \quad (6)$$

It can be seen that the electrons are scattered away while moving in the self-generated B-field, and so one always has $v_{r0}A_r > 0$ if it is taken that $A_r(+\infty) = 0$. Thus, one can expect the magnetized electrons to experience an equivalent drag force in the longitudinal direction, leading to a reduction in the electric potential.

To analyze the magnetization effect more quantitatively, in principle we need self-consistent solutions for both ϕ and A_r. However, it does not seem possible to obtain such solutions, since the magnetic field generation is a multidimensional problem. To proceed further, therefore, we assume that the self-similar behavior of the magnetic potential is approximately the same as that of the electric potential. This is a reasonable assumption, because both the magnetic and electric fields stem from the same source, namely, the ejection of hot electrons. Therefore, we assume $A_r(\xi) = -\alpha\phi(\xi)$, where $\alpha > 0$ is a constant. Here, α also represents the ratio between the strength of the azimuthal magnetic field and that of the electric field, i.e., $\alpha \equiv c|B_\theta|/|E_z|$. Under this assumption, Eq. (6) becomes the Boltzmann relation

$$n_e = n_{e0}\exp[(1 + v_{r0}\alpha)\phi]. \quad (7)$$

Next, we consider the ion fluid motion in the electric potential. The equations of continuity and motion for the initially cold ions are

$$\frac{\partial n_i}{\partial t} + \frac{\partial(n_i v_{iz})}{\partial z} = 0, \quad (8)$$

$$\frac{\partial v_i}{\partial t} + v_{iz}\frac{\partial v_{iz}}{\partial z} = -\frac{Ze}{m_i}\frac{\partial \phi}{\partial z}, \quad (9)$$

where v_{iz} is the longitudinal velocity of the ions. Using the self-similar variable $\xi = z/t$ and the normalized quantity $v_{iz} = v_{iz}/c_s$, Eqs. (8) and (9) become

$$(v_{iz} - \xi) \frac{d \ln n_i}{d\xi} = -\frac{dv_{iz}}{d\xi}, \tag{10}$$

$$(v_{iz} - \xi) \frac{dv_{iz}}{d\xi} = -\frac{d\phi}{d\xi}. \tag{11}$$

Now using the quasineutrality assumption $n_e = Z n_i$, we easily obtain the self-similar solutions of Eqs. (10) and (11):

$$v_{iz} = \xi + \frac{1}{(1 + v_{r0}\alpha)^{1/2}}, \tag{12}$$

$$\phi = -\frac{1}{(1 + v_{r0}\alpha)^{1/2}} (\xi + 1), \tag{13}$$

$$n_i = n_{i0} \exp\left[-(1 + v_{r0}\alpha)^{1/2} (\xi + 1)\right]. \tag{14}$$

If $B_\theta = 0$ (or $\alpha = 0$), then Eqs. (12)–(14) become the well-known self-similar solutions of the electrostatic model.[28]

In the presence of a B-field, the rate of reduction in ion energy caused by the B-field can be estimated as

$$\frac{\delta \mathcal{E}_i}{\mathcal{E}_i} = \frac{\phi_0 - \phi}{\phi_0} = 1 - \frac{1}{(1 + v_{r0}\alpha)^{1/2}}, \tag{15}$$

where $\phi_0 = -(\xi + 1)$ is the electric potential in the electrostatic case. Equation (15) shows that the ion energy will be reduced as a result of a decrease in electric potential. If $\alpha \equiv c|B_\theta|/|E_z| \gg 1$, then the electric potential will be completely suppressed, i.e., $\phi = 0$, and no ion acceleration will occur. However, in a realistic TNSA scenario, the field strength of the self-generated B_θ is usually less than that of the sheath field E_z, i.e., $\alpha \leq 1$, even at high laser intensities. To estimate v_{r0}, we note that the fast electrons are dispersed within a cone of half-angle 30°, as observed in most experiments.[31,32] This corresponds to an average perpendicular velocity of $v_{r0} = 0.25c$ if a uniform distribution in the cone angle is assumed. The rate of reduction in ion energy is then estimated, using $\alpha = 1$ and $v_{r0} = 0.25c$, to be only $\delta \mathcal{E}_i/\mathcal{E}_i \sim 10\%$. This energy reduction by the magnetization effect may be overestimated, because the B-fields in general have a longer growth time than the sheath E-fields. Therefore, the protons can be accelerated promptly before the electron trajectories are strongly perturbed by the B-field. Furthermore, other effects, such as a reduction in deflection due to inhibition of the transverse sheath field, are also expected to compensate for the energy reduction. Therefore, one can conclude that the magnetization effect in a realistic TNSA scenario should not be strong enough to significantly inhibit the sheath acceleration of high-energy protons.

IV. INHIBITED ION ACCELERATION AT HIGH LASER INTENSITIES

The above considerations suggest that the magnetization effect plays a rather limited role in hampering ion acceleration, and hence it cannot explain the degraded scaling of the maximum proton energy with increasing laser intensity that is observed in both the PIC simulations and experimental results.[33,34] To gain a more complete understanding of the inhibited ion acceleration at high laser intensities, we also carry out 2D PIC simulations in which the laser

intensity is varied over three orders of magnitude while the target parameters and the other laser parameters are kept fixed at the same values as in the preceding simulations. The maximum proton energy $\mathcal{E}_i^{max}$ and the maximum sheath field strength E_s^{max} are shown as functions of the peak laser intensity in Fig. 5. As is well known, in TNSA, the accelerating sheath field is given approximately by $E_s^{max} = eT_h/L_s$, where T_h is the hot-electron temperature and L_s is the typical spatial extension of the sheath.[8] T_h is given by the ponderomotive scaling law,[35] $T_h = m_e^2 [(1 + a_0^2/2)^{1/2} - 1]$, and L_s can be estimated as the Debye length of the hot electrons, $\lambda_{Dh} = (T_h/4\pi e^2 n_h)^{1/2}$, where n_h is the hot-electron density. Recalling the energy conversion law $\eta_h I_L = n_h T_h$, where η_h is the laser absorption at the front of the target, we immediately obtain $E_s^{max} = (4\pi n_h T_h)^{1/2} \propto (\eta_h I_L)^{1/2}$. An ion crossing the sheath then acquires an energy $\mathcal{E}_i^{max} \sim Z e E_s^{max} L_s = Z T_h \propto I_L^{1/2}$ (where Z is the charge state of the ion), as is expected. Figure 5 shows that the sheath field strength E_s^{max} has a scaling $\propto I^{0.4-0.66}$, which is close to the rough prediction above. In particular, the maximum sheath field E_s^{max} in the low-intensity regime 10^{20} W cm$^{-2} < I_L < 10^{22}$ W cm^{-2} grows according to an effective power law $\propto (I_L\lambda^2)^{0.4}$, while the scaling increases to $\propto (I_L\lambda^2)^{0.66}$ in the high-intensity regime 10^{22} W cm$^{-2} < I_L < 10^{23}$ W cm^{-2}. The better scaling of E_s^{max} at high laser intensities can be attributed to the increased absorption caused by hole boring at the front of the target. If a hole is formed, Brunel-type absorption may take place along the side, and the $\mathbf{J} \times \mathbf{B}$ mechanism may be enhanced owing to the additional self-focusing of the laser light. The better scaling of E_s^{max} also confirms that the sheath field will not be weakened by the magnetization effect, even at high laser intensities.

In contrast to the sheath field E_s^{max}, the scaling of the maximum proton energy $\mathcal{E}_i^{max}$ becomes poorer at high laser intensities. In particular, $\mathcal{E}_i^{max}$ scales as $\propto (I_L\lambda^2)^{0.71}$ in the low-intensity regime, while it drops to $\propto (I_L\lambda^2)^{0.34}$ in the high-intensity regime. The poorer scaling of proton energy at high laser intensities can in fact be explained well by the limited acceleration time of protons in the
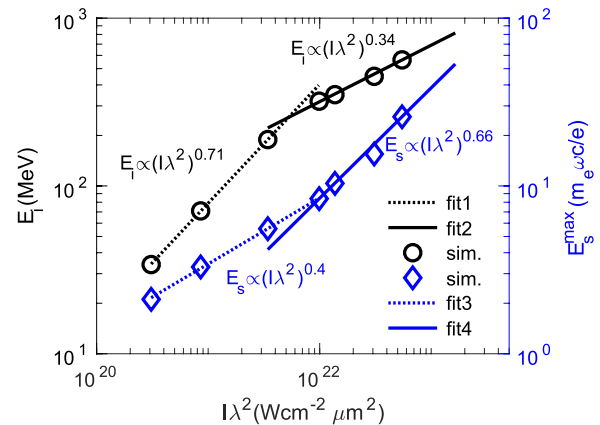

FIG. 5. Maximum proton energy $\mathcal{E}_i^{max}$ and maximum sheath field strength E_s^{max} as functions of the peak laser intensity. The circles and diamonds are the results from the 2D PIC simulations. The fitted curve segments for the proton energy shown by the dashed and solid black lines satisfy $\mathcal{E}_i \propto (I\lambda^2)^{0.71}$ and $\mathcal{E}_i \propto (I\lambda^2)^{0.34}$, respectively. The other two fitted curve segments shown by the dashed and solid blue lines satisfy $E_s \propto (I\lambda^2)^{0.4}$ and $E_s \propto (I\lambda^2)^{0.66}$, respectively.

sheath field, rather than by the magnetization effect, as was previously believed. The acceleration of the protons is limited by a time of the order of the pulse duration, $t_{acc,1} \approx \tau_L$, or by the time at which the proton position x_i exceeds the spatial extension of the sheath L_s, $t_{acc,2} \approx (2L_s m_i / Ze E_s^{max})^{1/2}$, depending on whichever is earlier. The threshold for the transition of the acceleration time can be estimated by $t_{acc,2} \approx t_{acc,1}$, or $E_s^{thr} \approx 2L_s m_i / Ze\tau_L^2$. Taking a pulse duration of $\tau_L = 50T_0$ as used in the simulations and $L_s \approx 5\lambda$, we have $E_s^{thr} \approx 1.2 m_e \omega c / e$, which is easily exceeded at high laser irradiances $I\lambda^2 \geq 3 \times 10^{20}$ W cm^{-2} (see Fig. 5). Therefore, at high laser intensities beyond this threshold, the proton acceleration is limited by the acceleration time within the extent of the sheath. Since the acceleration time in this regime decreases with increasing strength of the sheath field, one can expect reduced scaling of the proton energy at high laser intensities.

V. CONCLUSION

PIC simulations have been used to study the effects of a spontaneous surface B-field on proton acceleration at high laser intensities. Magnetization effects of the self-generated B-field are observed, but are not strong enough to affect sheath-driven proton acceleration, especially in realistic TNSA scenarios. A considerable reduction in proton energy is observed when an intense external B-field is present and the Lorentz force on a charged particle becomes much more intense than in the case of TNSA, but this may not occur in realistic scenarios. Also, it is found that since the gyro-motion of electrons in the self-generated B-field tends to suppress the growth of a transverse sheath field, deflection of low-energy protons by the latter field is prevented. As a result, the divergence of low-energy protons is actually increased by the self-generated B-field.

A theoretical model including the $\mathbf{v} \times \mathbf{B}$ force has also been presented to estimate the magnetization effect on proton acceleration. It is found that the reduction in the proton energy depends on the strength ratio between B_s and E_s rather than on the strength of B_s alone. For typical values of $cB_s \sim E_s$ in TNSA, the analysis confirms that only a few percent of the proton energy will be affected by a self-generated B-field.

Finally, it has been argued that the degraded scaling of proton energy at high laser intensities can be attributed to the magnetization effect of the self-generated B-field. In fact, our PIC results presented here indicate better scaling of the sheath field at higher laser intensities, and thus cannot support the view that the sheath field is inhibited by strong magnetization effects. Instead, it has been shown that the degraded scaling of proton energy can be reasonably explained by the decreased acceleration time due to the increased sheath field at high laser intensities. This more complete understanding of the magnetization effect on ion acceleration will have important implications for the design of ion sources at upcoming multi-PW laser facilities.[36–38]

DATA AVAILABILITY

The data that support the findings of this study are available from the corresponding author upon reasonable request.

REFERENCES

[1]A. Yogo, K. Sato, M. Nishikino et al., "Application of laser-accelerated protons to the demonstration of DNA double-strand breaks in human cancer cells," Appl. Phys. Lett. **94**, 181502 (2009).

[2]K. Zeil, M. Baumann, E. Beyreuther et al., "Dose-controlled irradiation of cancer cells with laser-accelerated proton pulses," Appl. Phys. B **110**, 437–444 (2013).

[3]H. Chen, S. C. Wilks, J. D. Bonlie et al., "Making relativistic positrons using ultraintense short pulse laser," Phys. Plasmas **16**, 122702 (2009).

[4]M. Roth, I. Alber, V. Bagnoud et al., "Proton acceleration experiments and warm dense matter research using high power lasers," Plasma Phys. Controlled Fusion **51**, 124039 (2009).

[5]M. Roth, T. E. Cowan, M. H. Key et al., "Fast ignition by intense laser-acceleated proton beams," Phys. Rev. Lett. **86**, 436–439 (2001).

[6]J. C. Fernández, J. J. Honrubia, B. J. ALbright et al., "Progress and prospects of ion-driven fast ignition," Nucl. Fusion **49**, 065004 (2009).

[7]J. C. Fernández, B. J. ALbright, F. N. Beg et al., "Fast ignition with laser-driven proton and ion beams," Nucl. Fusion **54**, 054006 (2014).

[8]A. Macchi, M. Borghesi, and M. Passoni, "Ion acceleration by superintense laser-plasma interaction," Rev. Mod. Phys. **85**, 751–793 (2013).

[9]B. Qiao, M. Zepf, M. Borghesi et al., "Stable GeV ion-beam acceleration from thin foils by circularly polarized laser pulse," Phys. Rev. Lett. **102**, 145002 (2009).

[10]T.-P. Yu, A. Pukhov, G. Shvets et al., "Stable laser-driven proton beam acceleration from a two-ion species ultra thin foil," Phys. Rev. Lett. **105**, 065002 (2010).

[11]S. C. Wilks, A. B. Langdon, T. E. Cowan et al., "Energetic proton generation in ultra-intense laser-solid interactions," Phys. Plasma **8**, 542 (2001).

[12]B. M. Hegelich, B. J. Albright, J. Cobble et al., "Laser acceleration of quasi-monoenergetic MeV ion beams," Nature **439**, 441–444 (2006).

[13]F. Wagner, O. Deppert, C. Brabetz et al., "Maximum proton energy above 85 MeV from the relativistic interaction of laser pulses with micrometer thick CH$_2$ targets," Phys. Rev. Lett. **116**, 205002 (2016).

[14]A. Higginson, R. J. Gray, M. King et al., "Near-100 MeV protons via a laser-driven transparency-enhanced hybrid acceleration scheme," Nat. Commun. **9**, 724 (2018).

[15]M. Nakatsutsumi, Y. Sentoku, A. Korzhimanov et al., "Self-generated surface magnetic fields inhibit laserdriven sheath acceleration of high-energy protons," Nat. Commun. **9**, 280 (2018).

[16]M. Nakatsutsumi, A. Kon, S. Buffechoux et al., "Fast focusing of short-pulse lasers by innovative plasma optics toward extreme intensity," Opt. Lett. **35**, 2314–2316 (2010).

[17]W. Schumaker, N. Nakanii, C. McGuffey et al., "Ultrafast electron radiography of magnetic fields in high-intensity laser-solid interactions," Phys. Rev. Lett. **110**, 015003 (2013).

[18]B. Albertazzi, S. N. Chen, P. Antici et al., "Dynamics and structure of self-generated magnetics fields on solids following high contrast, high intensity laser irradiation," Phys. Plasma **22**, 123108 (2015).

[19]Z. M. Zhang, X. T. He, Z. M. Sheng et al., "Hundreds MeV monoenergetic proton bunch from interaction of 10^{20-21} W/cm^2 circularly polarized laser pulse with tailored complex target," Appl. Phys. Lett. **100**, 134103 (2012).

[20]P. Mora, "Plasma expansion into a vacuum," Phys. Rev. Lett. **90**, 185002 (2003).

[21]J. Fuchs, P. Antici, E. d'Humières et al., "Laser-driven proton scaling laws and new paths towards energy increase," Nat. Phys. **2**, 48–54 (2006).

[22]M. G. Haines, "Saturation mechanisms for the generated magnetic field in nonuniform laser-matter irradiation," Phys. Rev. Lett. **78**, 254–257 (1997).

[23]F. Califano, F. Pegoraro, and S. V. Bulanov, "Spatial structure and time evolution of the Weibel instability in collisionless inhomogeneous plasmas," Phys. Rev. E **56**, 963–969 (1997).

[24]P. Antici, L. Gremillet, T. Grismayer et al., "Modeling target bulk heating resulting from ultra-intense short pulse laser irradiation of solid density targets," Phys. Plasma **20**, 123116-1–123116-8 (2013).

[25]M. Passoni and M. Lontano, "One-dimensional model of the electrostatic ion acceleration in the ultraintense laser–solid interaction," Laser Particle Beams **22**, 163–169 (2004).

[26]M. Passoni and M. Lontano, "Theory of light-ion acceleration driven by a strong charge separation," Phys. Rev. Lett. **101**, 115001 (2008).

[27]M. Passoni, L. Bertagna, and A. Zani, "Energetic ions from next generation ultraintense ultrashort lasers: Scaling laws for target normal sheath acceleration," Nucl. Instrum. Methods Phys. Res., Sect. A **620**, 46–50 (2010).

[28]P. Mora and R. Pellat, "Self-similar expansion of a plasma into a vacuum," Phys. Flusids **22**, 2300 (1979).

[29]J. E. Crow, P. L. Auer, and J. E. Allen, "Expansion of a plasma into a vacuum," J. Plasma Phys. **14**, 65–76 (1975).

[30]Y. Omura, Y. Katoh, and D. Summers, "Theory and simulation of the generation of whistler-mode chorus," J. Geophys. Res. **113**, A04223, https://doi.org/10.1029/2007ja012622 (2008).

[31]A. Debayle, J. J. Honrubia, E. d'Humières et al., "Divergence of laser-driven relativistic electron beams," Phys. Rev. E **82**, 036405 (2010).

[32]V. Ovchinnikov, D. W. Schumacher, M. Mcmahon et al., "Effects of preplasma scale length and laser intensity on the divergence of laser generated hot electrons," Phys. Rev. Lett. **110**, 065007 (2013).

[33]M. Borghesi, A. Bigongiari, S. Kar et al., "Laser-driven proton acceleration: Source optimization and radiographic applications," Plasma Phys. Controlled Fusion **50**, 124040 (2008).

[34]M. Borghesi, J. Fuchs, S. V. Bulanov et al., "Fast ion generation by high-intensity laser irradiation of solid targets and applications," Fusion Sci. Technol. **49**, 412–439 (2006).

[35]S. C. Wilks, W. L. Kruer, M. Tabak et al., "Absorption of ultra-intense laser pulses," Phys. Rev. Lett. **69**, 1383–1386 (1992).

[36]Z. Guo, L. H. Yu, J. Y. Wang et al., "Improvement of the focusing ability by double deformable mirrors for 10-PW-level Ti: Sapphire chirped pulse amplification laser system," Opt. Express **26**, 026776 (2018).

[37]J. W. Yoon, C. Jeon, J. Shin et al., "Achieving the laser intensity of 5.5×10^{22} W/cm^2 with a wavefront-corrected multi-PW laser," Opt. Express **27**, 020412 (2019).

[38]X. M. Zeng, K. N. Zhou, Y. L. Zuo et al., "Multi-petawatt laser facility fully based on optical parametric chriped pulse amplification," Opt. Lett. **42**, 2014 (2017).